ENVIRONMENTAL RESEARCH
LETTERS

LETTER • OPEN ACCESS

# COVID-19 lockdown air quality change implications for solar energy generation over China

To cite this article: Kelvin Tsz Hei Choi and Helen Brindley 2021 *Environ. Res. Lett.* **16** 024029

ENVIRONMENTAL RESEARCH
LETTERS

CrossMark

OPEN ACCESS

RECEIVED
12 August 2020

REVISED
25 November 2020

ACCEPTED FOR PUBLICATION
16 December 2020

PUBLISHED
29 January 2021



LETTER

# COVID-19 lockdown air quality change implications for solar energy generation over China

**Kelvin Tsz Hei Choi**[1,2] and **Helen Brindley**[1,2]

[1] Space and Atmospheric Physics Group, Imperial College London, London SW7 2AZ, United Kingdom
[2] National Centre for Earth Observation, Imperial College London, London SW7 2AZ, United Kingdom

**E-mail:** thc313@ic.ac.uk

**Keywords:** earth observation, COVID-19 lockdown, air quality, nitrogen dioxide, aerosol, solar energy, multi-junction

## Abstract

We exploit changes in air quality seen during the COVID-19 lockdown over China to show how a cleaner atmosphere has notable co-benefits for solar concentrator photovoltaic energy generation. We use satellite observations and analyses of the atmospheric state to simulate surface broadband and spectrally resolved direct normal irradiance (DNI). Over Wuhan, the first city placed under lockdown, we show how the atmospheric changes not only lead to a 19.8% increase in broadband DNI but also induce a significant blue-shift in the DNI spectrum. Feeding these changes into a solar cell simulator results in a 29.7% increase in the power output for a typical triple-junction photovoltaic cell, with around one-third of the increase arising from enhanced cell efficiency due to improved spectral matching. Our estimates imply that these increases in power and cell efficiency would have been realised over many parts of China during the lockdown period. This study thus demonstrates how a cleaner atmosphere may enable more efficient large scale solar energy generation. We conclude by setting our results in the context of future climate change mitigation and air pollution policies.

## 1. Introduction

The COVID-19 lockdown over China led to a dramatic reduction in economic activity within the country. The imposed travel restrictions and quarantines led to a drop in nitrogen dioxide ($NO_2$) emissions by 30%–60% [1–4]. Changes in aerosol loading and characteristics, which may be partially attributable to lockdown restrictions, also occurred [5, 6]. In this study we translate these changes in air quality into their impact on the performance of multi-junction (MJ) solar cells, focusing on the effects of changes in $NO_2$ concentration and aerosol optical depth (AOD). Whilst the impact on health from the air quality improvement due to the lockdown has already been quantified [7], understanding other potential co-benefits is of interest given the effects that proposed climate change mitigation policies [8] will have on atmospheric composition [9]. Although changes in emissions due to the lockdown will likely be temporary as economic activities resume, this investigation provides an insight into how future changes in air quality could have a significant impact on solar cell efficiency and hence large scale energy generation.

Specifically, we examine the behaviour of a commercially available, highly efficient, triple junction InGaP/InGaAs/Ge (MJ) solar cell typically used in concentrator photovoltaic systems (CPV) [10]. Due to their concentrating optics, CPV systems can only accept direct normal irradiance (DNI) and not the global irradiance. Given their MJ architecture, meaning each layer of the cell is designed to absorb a specific part of the spectrum, MJ CPV are more spectrally sensitive than conventional single-junction cells. As such, they are particularly susceptible to changes in atmospheric conditions, since variations in aerosols, water vapour and trace gas concentrations all alter the shape of the solar spectrum at the surface [11–15]. Indeed, several studies have considered the spectral impact of varying airmass, AOD and precipitable water on MJ CPV performance [16–19], though, to the best of our knowledge, none have explicitly analysed the effects of changes in short-lived pollutants such as $NO_2$.

This paper is organised as follows. In section 2, we examine changes in $NO_2$ and aerosols over China during the lockdown period from satellite observations and atmospheric analyses. In section 3, we describe the radiative transfer and solar cell simulation tools we employ to estimate changes in solar cell performance. Focusing on Wuhan as a first case study, in sections 4.1 and 4.2, we present the simulated changes in spectral DNI and power output, respectively, before highlighting results from other cities. In section 4.3 we widen our analysis to the entire Chinese mainland before concluding with section 5.

## 2. Observations and analyses

We examine changes in solar energy-relevant atmospheric species during the lockdown over China. The lockdown coincided with the Chinese Lunar New Year holiday (25 January 2020), which would have seen reductions in economic activities regardless of lockdown restrictions [20]. Therefore, one needs to be cautious when selecting a baseline period for comparison. Further, lockdowns were staggered across China, with restrictions across many provinces not reaching full force until February [5]. Considering this, and the timing of the Chinese New Year in 2019, we compare 15 February to 15 March 2019 to the same period in 2020. Selecting the same time of year for comparison also reduces the influence of seasonal effects. Hereafter, we abbreviate 15 February to 15 March as Feb/Mar.

### 2.1. Changes in nitrogen dioxide

We use the $NO_2$ daily product from the offline stream of total columnar measurements from the TROPOspheric Monitoring Instrument (TROPOMI) [21]. TROPOMI has a spatial resolution of 5.5 km $\times$ 3.5 km at nadir, suitable for identifying city-scale $NO_2$ levels. As $NO_2$ exhibits a strong diurnal cycle [22], these measurements are only representative of the concentration level at the satellite overpass time (1330 LST). We grid the data to $0.05^\circ \times 0.05^\circ$ and create a monthly average for each Feb/Mar period (figure 1). Only data with a quality assurance greater than 0.75 are included. Total columnar $NO_2$ from TROPOMI has been validated against ground-based observations with differences typically within $\pm$10% for locations experiencing clean to moderately polluted conditions [23, 24], but with negative biases of up to 50% seen over heavily polluted cities [25]. However, since we are considering differences here, systematic biases will cancel to first order both in the concentration changes and in their propagation to changes in solar radiation.

Although TROPOMI shows the expected meteorologically induced seasonal peak in $NO_2$ during winter [26, 27], figures 1(a)–(c) highlights a marked decrease in monthly Feb/Mar $NO_2$ in 2020 compared to 2019. Although not shown here, this drop persists from January to March 2020 before $NO_2$ concentrations rise again towards April 2020 as some cities emerge from lockdown. The reduced $NO_2$ emission has been attributed to the reduction of fossil-fuel-based activity, such as road traffic, industry, coal-fired power plants and aviation [5].

Figure 1(d) compares the columnar $NO_2$ above major Chinese cities for the two Feb/Mar periods. To produce these estimates, we average pixels within a 15 km radius around each city centre. We observe a consistent decrease in $NO_2$ for all of these locations. Wuhan, one of the first cities placed under lockdown, saw the most dramatic reduction at 75%, but reductions of between 25% and 50% are commonplace across a large number of cities. These changes are comparable to those seen from point, ground-based observations, which suggest 50%–60% reductions over Wuhan and 40% reductions over Beijing [3]. While meteorological fields such as the boundary layer height, wind speed and relative humidity may affect $NO_2$ concentrations, recent studies [7] have indicated that a significant portion of the change is related to the lockdown.

### 2.2. Changes in aerosols

We use AOD measurements from the MODerate Resolution Imaging Spectroradiometer (MODIS). AOD is a measure of the abundance of suspended particles and droplets, of natural or anthropogenic origin, in the atmosphere. We use the collection 6.1 dark target level 2 product over land (MYD04 L2) [28], regridded to $0.1^\circ \times 0.1^\circ$ and averaged across the same period as the $NO_2$ observations. Only Aqua measurements are included to ensure overpass time coincidence with TROPOMI. Previous studies suggest the MODIS collection 6.1 AOD product is reliable over inland areas covering the North China Plain and Central China [29], encompassing the region under investigation. In particular, they show a correlation of 0.82 over Wuhan.

Figures 2(a)–(c) shows AOD at 550 nm ($\tau_{550}$) from MODIS for Feb/Mar 2019 and 2020 and the 2020–2019 difference. Changes in $\tau_{550}$ are less uniform across China than those seen in $NO_2$. Whilst we observe a reduction in $\tau_{550}$ over central China, we see increases in the southwest and northeast. Figure 2(d) reiterates this impression. These variable $\tau_{550}$ changes are consistent with ground-based observations of $PM_{2.5}$ [3, 6]. Given the high inter-annual variability in AOD, the variety of natural and anthropogenic sources and the complex relationships between AOD and local meteorology, we make no attempt to directly attribute the changes seen here to lockdown measures.

The Angström exponent ($\alpha$) is a measure of the spectral variation of $\tau_\lambda$, and is a proxy for aerosol size distribution [30]. We compute $\alpha$ from MODIS AOD using:

$$\alpha_{\lambda_{1,2}} = -\frac{\log \frac{\tau_{\lambda_1}}{\tau_{\lambda_2}}}{\log \frac{\lambda_1}{\lambda_2}} \quad (1)$$

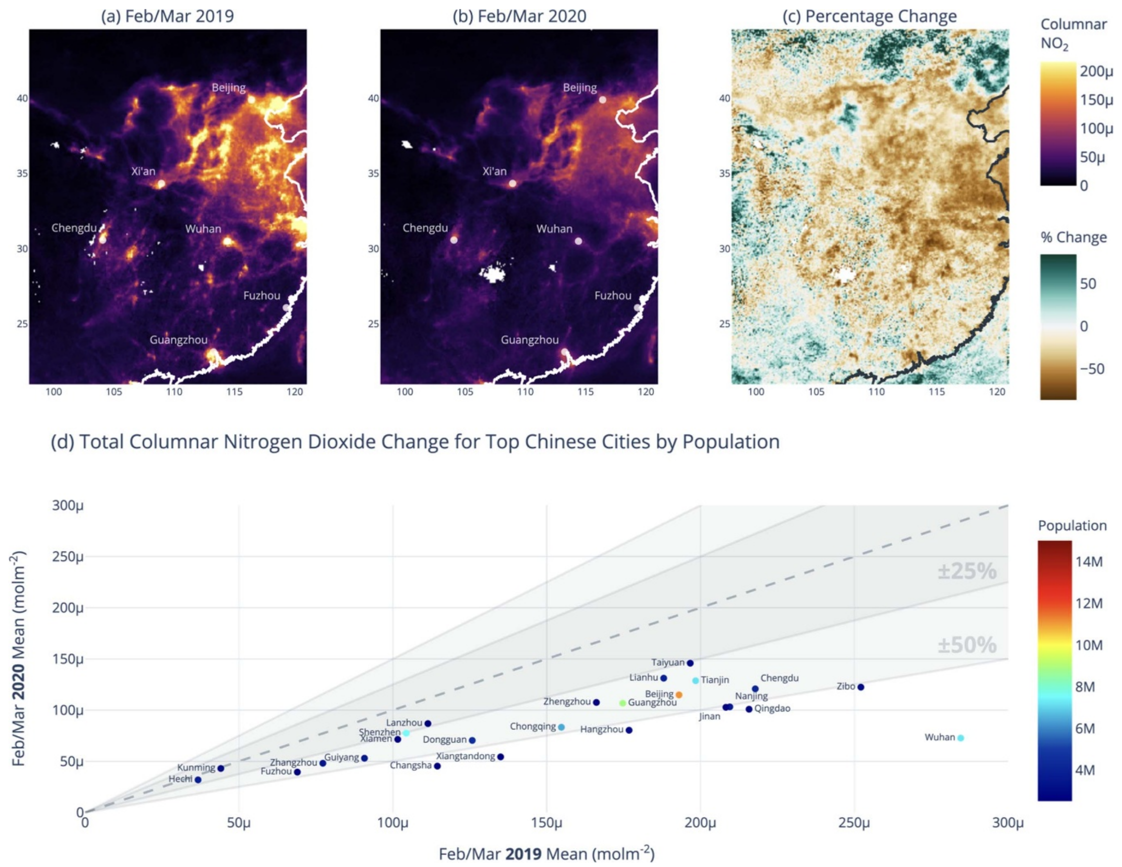


**Figure 1.** Averaged total columnar $NO_2$ over China from TROPOMI for (a) Feb/Mar 2019 and (b) Feb/Mar 2020. (c) Shows the percentage change between the periods, with a negative change implying a reduction in columnar $NO_2$ in 2020. The mean percentage change across all pixels within the study area with valid retrievals during both periods is −9.5%. (d) Compares the $NO_2$ levels for the largest Chinese cities by population within the study area. Shading indicates areas of up to ±25% and ±50% change.

where $\tau_{\lambda_1}$ and $\tau_{\lambda_2}$ are AODs measured at wavelengths $\lambda_1 = 470$ nm and $\lambda_2 = 660$ nm. In general, a higher $\alpha$ implies a more pronounced spectral variation and is indicative of finer aerosols such as urban anthropogenic aerosols. On the other hand, a lower $\alpha$ implies coarser aerosols, typically characteristic of aerosols of natural origin, such as desert dust or marine salts. As $\alpha$ is a measure of the spectral variation of aerosol extinction, many studies have shown that it has important effects on MJ CPV performance [17].

Similar to $\tau_{550}$, the spatial distribution of changes in $\alpha$ between Feb/Mar 2019 and 2020 is not uniform (not shown). Whilst $\alpha$ decreased substantially over Northern China, Central China experienced an increase in $\alpha$. As a specific example, Beijing saw a substantial reduction in $\alpha$, indicative of the presence of coarser aerosols. As such, not only did Beijing see an increase in aerosol loading (figure 2(d)), but the properties and therefore the origin of the aerosols is likely to have changed.

### 2.3. Vertical profiles and other species

Our radiative transfer calculations (section 3.1) require vertically resolved profiles of the relevant atmospheric species. For water vapour and $O_3$, we take profiles directly from the European Centre for Medium-Range Weather Forecasts Copernicus Atmosphere Monitoring Service (CAMS) [31] closest in time to the satellite overpasses (0600 UTC), and produce monthly averages at 0.5° × 0.5° over the relevant periods. For $NO_2$, we use the CAMS profiles scaled to the monthly averaged TROPOMI observations. For aerosols, we use the relevant optical properties of aerosol and cloud (OPAC) [32] types and scale height, scaled to the monthly averaged MODIS observations. $CO_2$ concentrations at ground are taken from measurements at NOAA's Earth System Research Laboratory at Mauna Loa [33].

Examining the monthly averaged profiles (not shown), we note a wetter atmosphere during the 2020 period over most parts of China. For instance, the averaged columnar water vapour number density increased by 29.4% over Wuhan. Meanwhile, columnar $O_3$ saw increases of up to 20% in northern China, but slight reductions (up to −4.4%) in the south between the two Feb/Mar periods.

## 3. Tools and simulations

### 3.1. Direct normal irradiance simulation

Spectral DNI is simulated with libRadtran [34] at 1 nm resolution with surface elevation taken from

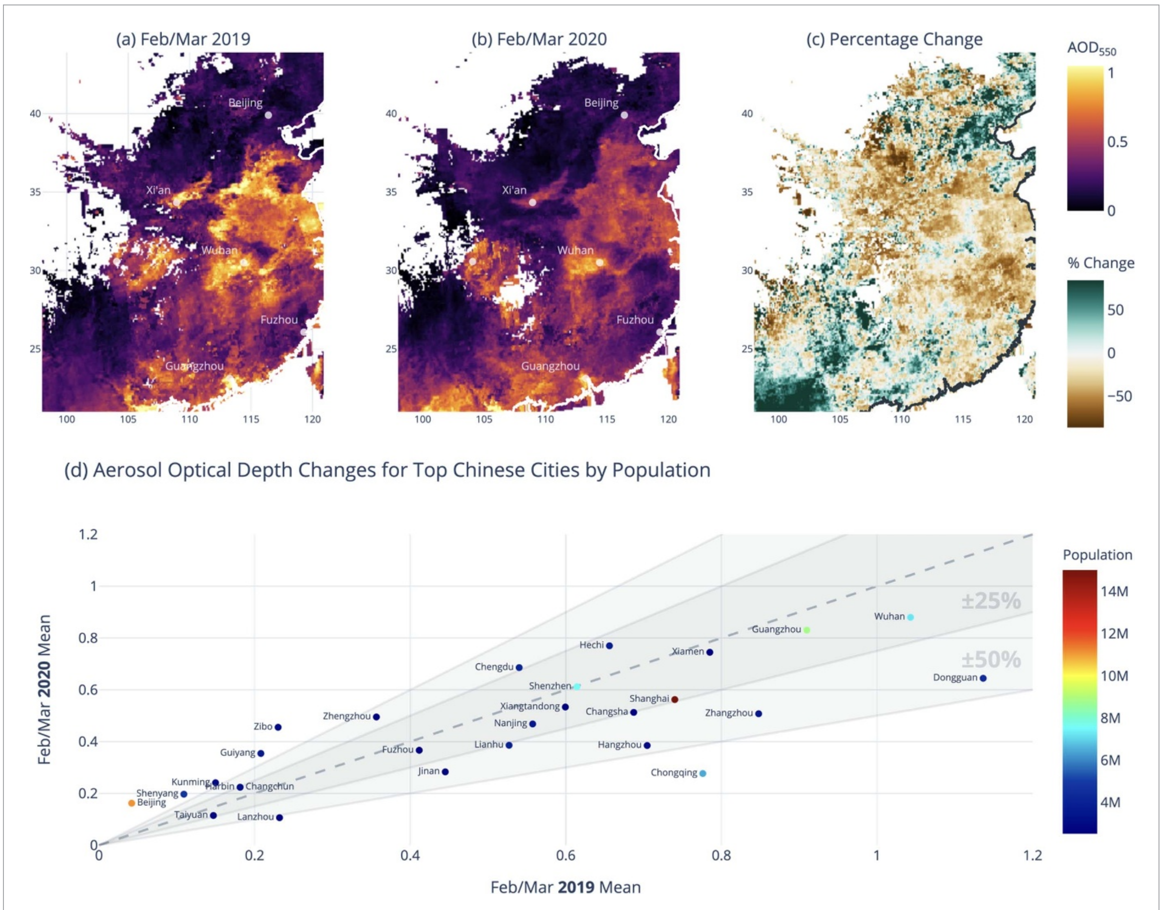


**Figure 2.** Feb/Mar $\tau_{550}$ from MODIS collection 6.1. (a), (b) Show $\tau_{550}$ for Feb/Mar 2019 and 2020 respectively. (c) Shows the percentage difference between the two. (d) Highlights the change between the 2019 and 2020 periods for major Chinese cities by population. Shading indicates areas of up to ±25% and ±50% change.

GMTED 2010 [35]. We use the Kurucz solar spectrum [36], scaled to the averaged total solar irradiance measurements from solar radiation and climate experiment [37] over the relevant periods to provide the solar spectrum at the top of the atmosphere.

Profiles of $NO_2$, $O_3$, $CO_2$, water vapour etc are taken from the observations and analyses described in section 2.3. However, for aerosol we include an additional step. We use the MODIS AOD measurements and their associated uncertainties at 470, 550 and 660 nm to determine the most appropriate aerosol type from one of ten types in the OPAC database [32] using least square fitting. This typing allows us to capture aerosol properties across solar energy-relevant wavelengths, up to 1.8 microns. We then use the optical properties of the selected OPAC type, with the measured MODIS $\tau_{550\,\mathrm{nm}}$, as input to the radiative transfer calculation. Our calculations also include the contribution from the circumsolar irradiance, assuming the CPV system has an aperture half angle of 2.5°.

We caveat that the DNI simulated from averaged AOD is not exactly the averaged DNI spectrum [38]. When the monthly average is used, we estimate an approximately 10% underestimation in broadband DNI compared to the averaged broadband DNI calculated from instantaneous AODs. However, the bias is systematic between the periods, meaning that it largely cancels when changes are considered.

### 3.2. Solar cell modelling

We make use of the solar cell simulator model Solcore [39]. The InGaP/InGaAs/Ge triple-junction (3J) CPV system follows the description in Rodrigo *et al* [14]. The 3J cell is topped with an MgF–ZnS anti-reflective coating. The stacked cell is solved optically with a transfer matrix method, and electrically with the depletion approximation. We fix the operating temperature of the cell at 300 K and scale the incident solar spectrum by a factor of 1000. Any spectral effects due to the CPV optics are ignored. The external quantum efficiency curves for the modelled cell are shown in figure 3. Over-plotted in red is the spectral location of the main $NO_2$ solar absorption band.

## 4. Results and analysis

We focus on Wuhan (30.5 °N, 114.4 °E) as the first case study to discuss our results. Referring to figures 1(c) and 2(d), relative to Feb/Mar 2019, Wuhan experienced a 75% decrease in columnar $NO_2$ in Feb/Mar 2020. The average $\tau_{550}$ of 1.043 during Feb/Mar 2019 is consistent with long term ground-based observations [42], while the equivalent value

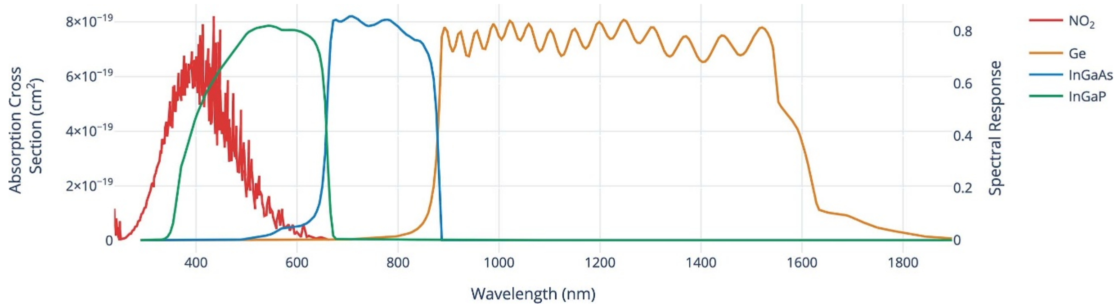


**Figure 3.** The spectral response for each of the three subcells of an InGaP/InGaAs/Ge triple-junction photovoltaic cell. Simulated using SolCore. Also shown is the absorption cross-section of $NO_2$ at 294 K in the UV and visible from the High-Resolution Transmission Molecular Absorption Database (HITRAN) [40, 41].

of 0.88 for Feb/Mar 2020 is lower than the spring climatological value by about 10%. $\alpha$ remained largely unchanged between the two periods.

### 4.1. Simulated direct normal irradiance

Figure 4(a) shows the simulated spectral DNI over Wuhan. Figure 4(c) indicates that the average broadband DNI available during Feb/Mar 2020 increased by 19.3% when compared to the same period in 2019, from 317.92 to 379.23 $\mathrm{Wm^{-2}}$. This is not surprising given the reduction in $NO_2$ concentration and AOD over the city.

Examining the difference spectra in figure 4(b), we note much of the gain occurs at shorter wavelengths, leading to a blue-shift in the spectrum. This blue shift can be quantified by the average photon energy (APE). APE is used to assess the spectral distribution of irradiance for solar energy applications [14, 43, 44]. It is the mean energy of all incoming photons in eV, defined as follows:

$$\mathrm{APE} = \frac{hc}{q\lambda_{\mathrm{eff}}} \qquad \lambda_{\mathrm{eff}} = \frac{\int \lambda \mathrm{DNI}_\lambda d\lambda}{\int \mathrm{DNI}_\lambda d\lambda} \qquad (2)$$

where $h$, $c$ and $q$ are the Planck constant, speed of light in vacuum and electronic charge respectively. In general, higher APEs are associated with bluer spectra. The APEs for the simulated spectra for Feb/Mar 2019 and 2020 are 1.23 and 1.29 eV respectively.

We break down the estimated 61.31 $\mathrm{Wm^{-2}}$ gain in DNI into the individual contributions from $NO_2$ and aerosol changes by inserting the 2020 profile for each variable, holding all other profiles at the 2019 level (figures 4(d) and (e)). Aerosol is the single most significant contributor to the overall increase in broadband DNI at +61.44 $\mathrm{Wm^{-2}}$. $NO_2$ contributes another +5.72 $\mathrm{Wm^{-2}}$. The umbrella 'other' term comprises changes in DNI that are not accounted for by either aerosols or $NO_2$, such as the effect of changes in water vapour, $O_3$ and $CO_2$. The increase in water vapour in 2020 noted previously leads to enhanced absorption in water vapour bands, seen in figure 4(d), reducing the DNI. This water vapour effect dominates this 'other' term, which contributes −6.47 $\mathrm{Wm^{-2}}$ to the change in broadband DNI.

Taken at face value, this might suggest that the increase in DNI resulting from the reduction in $NO_2$ is more than offset by the reduction in DNI due to the contributions from other absorbers. However, figure 4(d) shows the increase in DNI resulting from the reduction in $NO_2$ concentration is manifested at wavelengths shorter than 600 nm, consistent with the absorption cross-section of $NO_2$ (figure 3). Meanwhile, the reduction in DNI due to the residual contribution is predominantly manifested at wavelengths longer than 900 nm. This spectral separation is highly relevant for MJ solar cell performance, as discussed in the next section.

### 4.2. Simulated solar cell output and performance

The spectra in figure 4 are passed into SolCore to simulate the power output from our typical 3J CPV. The primary quantity of interest is the maximum power point (MPP, $P_m$), which is the maximum power deliverable from a cell given a particular irradiance spectrum. $P_m$ has the same $\mathrm{Wm^{-2}}$ unit as the incident broadband DNI but should be interpreted as the power output in Watt, per metre squared of solar panel. Importantly, in general, given a fixed spectral shape, $P_m$ is expected to vary approximately linearly over the range of DNI change under consideration here [45, 46].

Figure 5(a) compares $P_m$ for the two periods. We estimate a 29.7% increase in power output, markedly larger than the 19.3% increase in broadband DNI. The additional 10.4% increase is attributable to spectral effects. For clarity, we make the following distinction between 'broadband' and 'spectral' contributions. The former refers to changes in $P_m$ due solely to changes in the intensity. The latter refers to changes in $P_m$ due solely to changes in the spectral distribution. These two effects contribute 18.3 and 9.8 $\mathrm{Wm^{-2}}$ respectively, summing to the total $P_m$ increase of 28.1 $\mathrm{Wm^{-2}}$.

Similar to DNI, the increase in $P_m$ is broken down by atmospheric variable in figure 5(b). $NO_2$ has a broadband $P_m$ contribution of only 1.7 $\mathrm{Wm^{-2}}$.

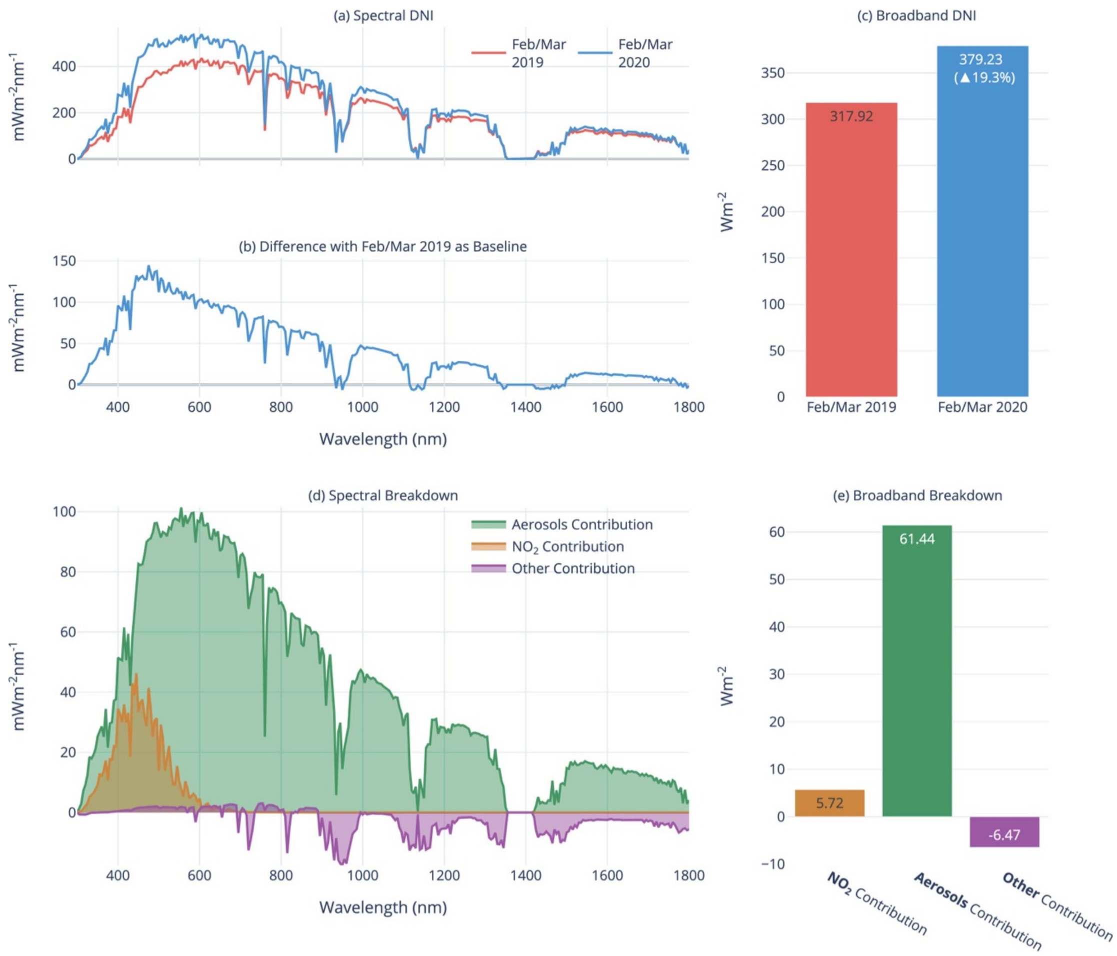


**Figure 4.** ((a) Simulated spectral DNI over Wuhan for the Feb/Mar period for 2019 and 2020. (b) Feb/Mar 2020-Feb/Mar 2019 spectral DNI difference. (c) Integrated broadband DNI for both periods in $Wm^{-2}$. Breakdown of the simulated (d) spectral and (e) broadband contribution to the DNI difference over Wuhan between Feb/Mar 2020 and 2019 for different atmospheric variables.

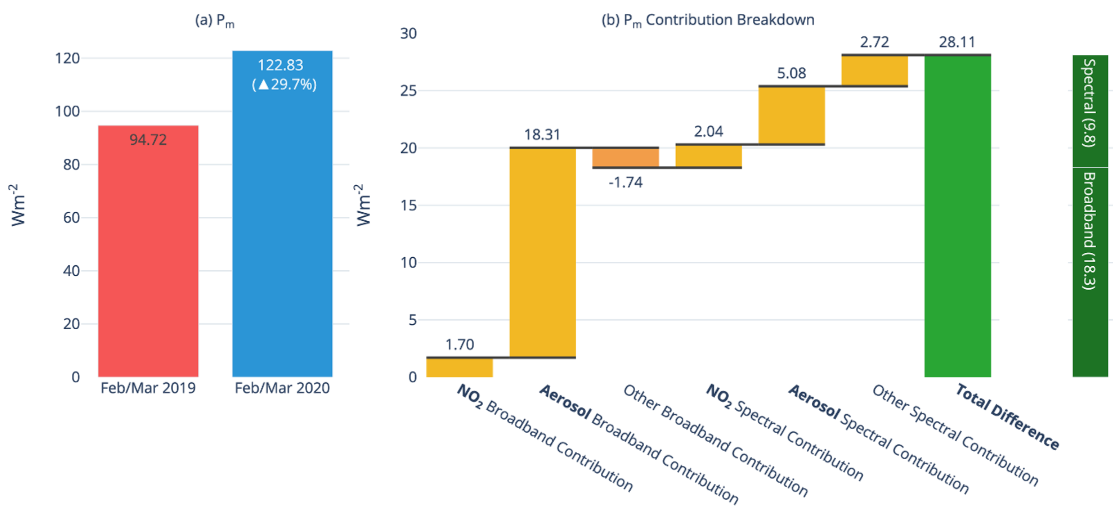


**Figure 5.** (a) Estimated maximum power point for an InGaP/InGaAs/Ge cell in CPV system during Feb/Mar 2019 and 2020 over Wuhan. (b) Total difference in estimated maximum power point between the two periods decomposed into broadband effects and spectral effects by atmospheric variable.

However, referring to figure 3, the absorption spectrum of $NO_2$ aligns well with the spectral range of the top InGaP layer of the 3 J CPV. Due to the in-series connection of the subcells, the overall current output of a MJ cell is always limited by the subcell that generates the smallest current, regardless

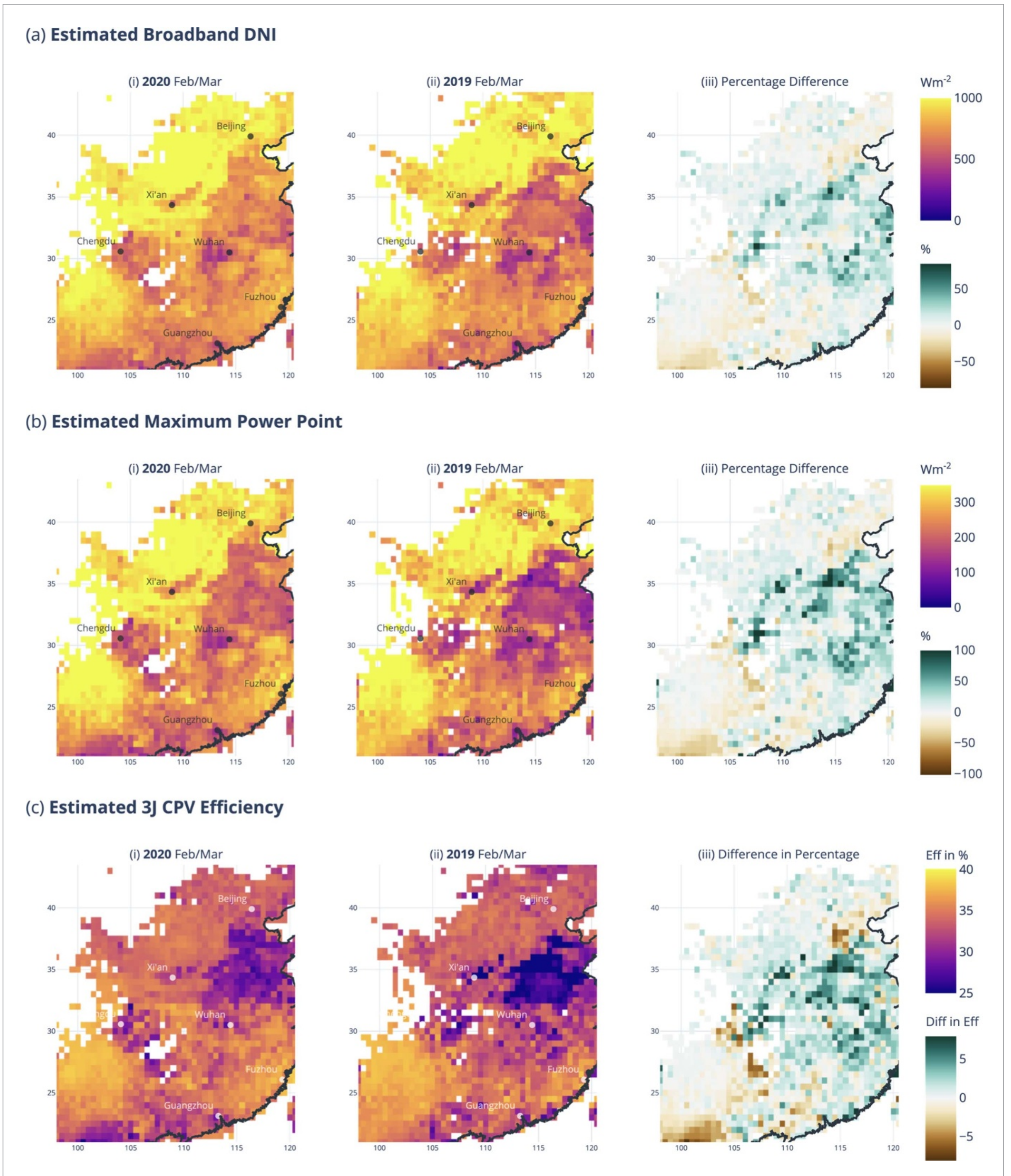


**Figure 6.** Simulated (a) broadband DNI, (b) maximum power point and (c) 3 J CPV cell efficiency, which is the ratio of (b) to (a), over China at 0.5° × 0.5° resolution. (i)s show the estimated values in Feb/Mar 2019 and (ii)s show the estimated values for Feb/Mar 2020. (iii)s show the percentage change between the two periods, with positive change indicating an increase in 2020. Only pixels with valid retrievals for both periods are included in (iii)s. The averaged percentage change for the whole scene is +4.7% for DNI (a(iii)); +8.5% for maximum power point (b(iii)) and +2.5% for cell efficiency (c(iii)).

of any surplus from other subcells. Here, it is the InGaP layer that is current-limiting and, as such, the reduction in $NO_2$ spectrally contributes an additional 2.04 $Wm^{-2}$ to the final power output. A similar spectral effect is seen for aerosols. Meanwhile, the contribution from other absorbers, whilst amounting to a broadband reduction of 1.7 $Wm^{-2}$, has a positive spectral contribution of 2.71 $Wm^{-2}$. This spectral gain occurs because the reduction is outside the wavenumber range relevant to the current limiting InGaP layer. Considering the normalised spectrum, so as to remove the broadband effect, this reduction is equivalent to a gain across the wavenumber range captured by the InGaP layer.

Another way of thinking about the spectral effect is in terms of cell efficiency. The simulated 3 J cell is spectrally tuned to the standard AM1.5d ASTM G-173-03 direct spectrum [47]. This standard DNI spectrum is derived from a pristine atmosphere with no $NO_2$ and assuming a rural aerosol type at low optical depth ($\tau_{500} = 0.084$). Under the illumination of such a spectrum, the cell operates at peak efficiency. Deviation from this reduces its performance.

Polluted urban environments, similar to that found over pre-lockdown Wuhan, have high aerosol loading and are predominately dominated by finer aerosols. This puts the cell under unfavourable operating conditions [17]. However, when the lockdown was in place, the cleaning of the atmosphere effectively transitioned the atmosphere over Wuhan into something closer to the standard atmosphere.

There are two ways to quantify this transition. First, we noted that the APE increased from 1.23 to 1.29 eV between the periods due to the spectral blue-shift (see figure 4(b)). This increase puts the APE during the Feb/Mar 2020 period closer to the APE of the standard spectrum, which is 1.4 eV. Alternatively, we may understand the spectral effect by looking at the simulated cell efficiency ($\eta$). $\eta$ is the ratio of $P_m$ to the incident broadband DNI. For Wuhan, we estimate an increase in cell efficiency of $\Delta\eta = 2.6\%$, from 29.8% to 32.4%. This improvement represents an approximately 9% increase in performance, translating to the 9.8 Wm$^{-2}$ increase in $P_m$ due to the improved spectral matching.

*4.2.1. Results for Shenzhen*

Like most areas of China, columnar $NO_2$ is reduced over Shenzhen (22.5°N, 114.1°E), a major economic hub in South China, in this case by 33.7%. The aerosol loading change, however, is minimal ($\Delta\tau_{550} < 0.01$). Nonetheless, a significant decrease in Angström exponent, from 1.47 to 0.87, augments the $NO_2$ induced blue-shift, with this shift translating to a 1.4% increase in APE. Indeed, although the broadband DNI only increases by 2%, $P_m$ increases by 5.2% due to the spectral effect. Hence, the spectral effect contributes more to the estimated power output increase than does the effect of increased broadband intensity.

*4.2.2. Results for Beijing*

Over Beijing (39.9°N, 116.4°E), we simulate an 11.6% decrease in broadband DNI despite a 39.5% reduction in columnar $NO_2$ over the city and a drop in $\alpha$ of similar magnitude to Shenzhen. The sign of the broadband DNI response is driven by an increase in $\tau_{550}$ from 0.042 to 0.162. This enhancement in AOD also more than counteracts the spectral shift induced by the reduction in both $NO_2$ and $\alpha$ such that the DNI spectrum becomes red-shifted. Overall, we estimate a reduction in cell efficiency, from 35.8% to 34.1%. The red-shift is also manifested in the APE, which is reduced by 2.3%. As such, the percentage reduction in $P_m$ is greater than that in the broadband DNI at −15.68%.

**4.3. Extension to mainland China**

Finally, for completeness, we widen our analysis, presenting maps of the broadband DNI, the MPP and the cell efficiency for Feb/Mar 2019 and 2020 with the corresponding differences over mainland China. The majority of the region analysed sees an increase in DNI, with some locations seeing an enhancement which exceeds 100% (figure 6(a)). Regions experiencing the most substantial broadband DNI increase are clustered around central China, consistent with areas experiencing the most significant decrease in $NO_2$ and $\tau_{550}$ (figures 1 and 2). Conversely, regions in the northeast and southwest show decreases in the available broadband DNI, mostly due to higher aerosol loading. The estimated $P_m$ for the 3 J CPV system follows a similar geospatial pattern to that for the broadband DNI. Again, we observe maximum increases exceeding 100% over central China (figure 6(b)). Figure 6(c) shows that cell efficiency is generally enhanced (by up to 14%) throughout central China due to the blue-shift of the spectral DNI induced by the $NO_2$ and $\tau_{550}$ changes. Corresponding plots of APE (not shown) show increases of up to 23%.

## 5. Discussions and conclusions

We combined satellite observations of atmospheric $NO_2$ concentrations and aerosol characteristics with atmospheric analyses to simulate the change in broadband and spectrally resolved surface DNI over China during the COVID-19 lockdown, comparing 15 February to 15 March 2019 against the same period in 2020. We then coupled these simulated changes with a solar cell model to estimate the impact on the output of a typical triple-junction cell used in concentrator photovoltaic systems (3 J CPV). Our motivation for this work was to investigate the impact of notable improvements in air-quality on solar energy generation potential.

Over Wuhan, the location of the first COVID-19 outbreak, satellite observations indicate a marked reduction in both $NO_2$ and AOD. This results in an increase in simulated broadband DNI of 19.8%. While the reduction in aerosol loading plays the dominant role in enhancing DNI, the spectral location of the main $NO_2$ absorption band, between 400 and 500 nm, is well-matched to the top, current-limiting cell in the 3 J CPV. Hence, the reduction in $NO_2$ introduces a notable blue-shift in the surface DNI spectrum, improving its spectral matching with the cell, enhancing cell efficiency and resulting in an overall increase in the cell MPP by 29.7%.

While the reduction in $NO_2$ is coherent across the Chinese mainland, the changes in aerosol loading are more variable and can induce reductions in DNI and mask the $NO_2$ impact on solar cell power enhancement over individual cities. Nevertheless, considering mainland China as a whole, our simulations show a mean increase of 8% in power output. Indeed, over much of central China, our simulations indicate similar spectral enhancements in 3 J CPV efficiency. We also note that although these efficiency estimates are tied to the specific cell design assumed in this study, the change in APE, a measure of the spectral distribution of irradiance for solar energy applications that is device independent, also indicates a marked blue-shift in the incident DNI spectrum across much of China. Given the likely locations of large-scale CPV installations are away from urban centres, this spatial coherence is important.

Although the changes in $NO_2$ emissions will likely be temporary as economic activities resume post-lockdown, this investigation provides an insight into how improvements in air quality could also benefit solar cell efficiency. Quantifying these 'hidden' benefits is particularly important in the context of the impact of proposed climate change mitigation policies and it is of interest to compare the observed changes over China during the COVID-19 lockdown to the scenarios laid out by the shared socioeconomic pathways (SSPs) [8]. This allows us to gain insight into how solar energy resources for MJ CPVs could evolve in the future.

The SSPs represent five different ways in which the world might unfold. In particular, SSP-1 describes a scenario where there are relatively optimistic trends for green development and human cooperation; SSP-2 represents the 'middle of the road' scenario, assuming continued historical patterns of development and; SSP-3 assumes a future where nations show little interest in working together to address global climate concerns. These pathways can be combined with mitigation targets defined in terms of the radiative forcing at 2100 to generate a wide range of possible scenarios as to how different levels of climate change mitigation can be achieved. The typical notation used to refer to a particular scenario is SSP-X-Y.Y where X is the SSP, and Y.Y is the radiative forcing in $Wm^{-2}$ in 2100. A recent paper by Lund *et al* [9] takes the SSP-1-1.9, SSP-2-4.5 and SSP-3-7.0 scenarios as input to a global chemistry-transport and radiative transfer model and estimates atmospheric gas concentrations and AOD levels in the future based on these scenarios. The difference in their calculated emissions of $NO_x$ between SSP-3-7.0 and SSP-2-4.5 by 2050 is similar to the average percentage difference in atmospheric $NO_2$ concentrations seen over China in this study ($\approx$35%). While the two measures are not directly comparable, this does show how climate change mitigation choices and the routes taken to achieve these will have marked implications for spectral DNI and hence MJ CPV energy generation. As such, this study highlights, based on real observations during the COVID-19 lockdown, the potential co-benefits that improving air quality could have in transitioning regions to be more suited for efficient, large scale solar energy generation.

Moreover, although we focus here on changes in clear-sky conditions during the lockdown, we also note a marked cloud fraction reduction (>50%) over many parts of China during the 2020 period based on the MODIS observations. While our discussions relate to increased instantaneous power production of 3 J CPV, the change in cloud statistics in favour of higher clear-sky frequency will further benefit the total energy yield of these 3 J CPV (and other photovoltaic) systems. Further work investigating the cause and effect of the aerosol and cloud changes is required to identify to what extent, if any, these can be tied to lockdown induced behaviour.

## Data availability statement

The data that support the findings of this study are available upon reasonable request from the authors.

## ORCID iD

Kelvin Tsz Hei Choi https://orcid.org/0000-0002-5796-5263

## References


[1] Zhang R *et al* 2020 Nox emission reduction and recovery during COVID-19 in East China *Atmosphere* **11** 433

[2] Bauwens M *et al* 2020 Impact of coronavirus outbreak on $NO_2$ pollution assessed using TROPOMI and OMI observations *Geophys. Res. Lett.* **47** e2020GL087978

[3] Shi X and Brasseur G P 2020 The response in air quality to the reduction of Chinese economic activities during the COVID-19 outbreak *Geophys. Res. Lett.* **47** e2020GL088070

[4] Silver B, He X, Arnold S R and Spracklen D V 2020 The impact of COVID-19 control measures on air quality in China *Environ. Res. Lett.* **15** 084021

[5] Filonchyk M, Hurynovich V, Yan H, Gusev A and Shpilevskaya N 2020 Impact assessment of COVID-19 on variations of $O_3$, $NO_2$, CO and AOD over East China *Aerosol Air Qual. Res.* **20** 1530–40

[6] He G, Pan Y and Tanaka T 2020 The short-term impacts of COVID-19 lockdown on urban air pollution in China *Nat. Sustain.* **3** 1005–11

[7] Cole M A, Elliott R J R and Liu B 2020 The impact of the Wuhan COVID-19 lockdown on air pollution and health: a machine learning and augmented synthetic control approach *Environ. Res. Econ.* **76** 553–80

[8] O'Neill B C *et al* 2017 The roads ahead: narratives for shared socioeconomic pathways describing world futures in the 21st century *Glob. Environ. Change* **42** 169–80

[9] Lund M T, Myhre G and Samset B H 2019 Anthropogenic aerosol forcing under the shared socioeconomic pathways *Atmos. Chem. Phys.* **19** 13827–39

[10] Nishioka K *et al* 2006 Annual output estimation of concentrator photovoltaic systems using high-efficiency InGaP/InGaAs/Ge triple-junction solar cells based on experimental solar cells characteristics and field-test meteorological data *Sol. Energy Mater. Sol. Cells* **90** 57–67

[11] Philipps S *et al* 2010 Energy harvesting efficiency of III–V triple-junction concentrator solar cells under realistic spectral conditions *Sol. Energy Mater. Sol. Cells* **94** 869–77

[12] Chan N L A *et al* 2012 Validation of energy prediction method for a concentrator photovoltaic module in Toyohashi Japan *Prog. Photovolt. Res. Appl.* **21** 1598–1610

[13] Behrendt T *et al* 2013 Solar spectral irradiance derived from satellite data: a tool to improve thin film PV performance estimations? *Sol. Energy* **98** 100–10

[14] Rodrigo P M, Fernández E F, Almonacid F M and Pérez-Higueras P J 2017 Quantification of the spectral coupling of atmosphere and photovoltaic system performance: indexes, methods and impact on energy harvesting *Sol. Energy Mater. Sol. Cells* **163** 73–90

[15] Caballero J A, Fernandez E F, Theristis M, Almonacid F and Nofuentes G 2018 Spectral corrections based on air mass, aerosol optical depth and precipitable water for PV performance modelling *IEEE J. Photovolt.* **8** 552–8
[16] Chan N L A, Brindley H E and Ekins-Daukes N J 2013 Impact of individual atmospheric parameters on CPV system power, energy yield and cost of energy *Prog. Photovolt. Res. Appl.* **22** 1080–95
[17] Fernández E F, Almonacid F, Ruiz-Arias J and Soria-Moya A 2014 Analysis of the spectral variations on the performance of high concentrator photovoltaic modules operating under different real climate conditions *Sol. Energy Mater. Sol. Cells* **127** 179–87
[18] Fernández E F, Soria-Moya A, Almonacid F and Aguilera J 2016 Comparative assessment of the spectral impact on the energy yield of high concentrator and conventional photovoltaic technology *Sol. Energy Mater Sol. Cells* **147** 185–97
[19] Theristis M, Fernandez E F, Stark C and O'Donovan T S 2016 A theoretical analysis of the impact of atmospheric parameters on the spectral, electrical and thermal performance of a concentrating III–V triple-junction solar cell *Energy Convers. Manage.* **117** 218–27
[20] Tan P-H, Chou C, Liang J-Y, Chou C C-K and Shiu C-J 2009 Air pollution 'holiday effect' resulting from the Chinese New Year *Atmos. Environ.* **43** 2114–24
[21] Veefkind J *et al* 2012 TROPOMI on the ESA sentinel-5 precursor: a GMES mission for global observations of the atmospheric composition for climate, air quality and ozone layer applications *Remote Sens. Environ.* **120** 70–83
[22] Han S *et al* 2011 Analysis of the relationship between $O_3$, NO and $NO_2$ in Tainjin, China *Aerosol Air Qual. Res.* **11** 128–39
[23] Ialongo I, Virta H, Eskes H, Hovila J and Douros J 2020 Comparison of TROPOMI/sentinel-5 precursor NO2 product with ground-based observations in Helsinki and first societal applications *Atmos. Meas. Tech. Discuss.* (https://doi.org/10.5194/amt-2019-329)
[24] Griffin D *et al* 2019 Highresolution mapping of nitrogen dioxide with TROPOMI: first results and validation over the Canadian Oil Sands *Geophys. Res. Lett.* **46** 1049–60
[25] Verhoelst T *et al* 2020 Ground-based validation of the copernicus sentinel-5p TROPOMI $NO_2$ measurements with the NDACC ZSL-DOAS, MAX-DOAS and Pandonia Global Networks *Atmos. Meas. Tech. Discuss.* **2020** 1–40
[26] Shah V *et al* 2020 Effect of changing $NO_x$ lifetime on the seasonality and long-term trends of satellite-observed tropospheric $NO_2$ columns over China *Atmos. Chem. Phys.* **20** 1483–95
[27] Zhang X, Zhang P, Zhang Y, Li X and Qiu H 2007 The trend, seasonal cycle and sources of tropospheric $NO_2$ over China during 1997–2006 based on satellite measurement *Sci. China* D **50** 1877–84
[28] Levy R C *et al* 2013 The collection 6 MODIS aerosol products over land and ocean *Atmos. Meas. Tech.* **6** 2989–3034
[29] Huang Y *et al* 2019 Evaluation and comparison of MODIS collection 6.1 and collection 6 dark target aerosol optical depth over mainland China under various conditions including spatiotemporal distribution, haze effects and underlying surface *Earth Space Sci.* **6** 2575–92
[30] Angstrom A 1961 Techniques of determining the turbidity of the atmosphere *Tellus* **13** 214–23
[31] Inness A *et al* 2019 The CAMS reanalysis of atmospheric composition *Atmos. Chem. Phys.* **19** 3515–56
[32] Hess M, Koepke P and Schult I 1998 Optical properties of aerosols and clouds: the software package OPAC *Bull. Am. Meteorol. Soc.* **79** 831–44
[33] Keeling C D *et al* 1976 Atmospheric carbon dioxide variations at Mauna Loa Observatory, Hawaii *Tellus* **28** 538–51
[34] Mayer B and Kylling A 2005 Technical note: the libRadtran software package for radiative transfer calculations—description and examples of use *Atmos. Chem. Phys. Discuss.* **5** 1319–81
[35] Danielson J J and Gesch D B 2011 Global multi-resolution terrain elevation data 2010 (GMTED2010) (Reston, VA: US Geological Survey) (https://pubs.usgs.gov/of/2011/1073/pdf/of2011-1073.pdf)
[36] Chance K and Kurucz R 2010 An improved high-resolution solar reference spectrum for earths atmosphere measurements in the ultraviolet, visible and near infrared *J. Quant. Spectrosc. Radiat. Transfer* **111** 1289–95
[37] Anderson D E and Cahalan R F 2005 *Solar Radiat. Clim. Exp. (SORCE)* (https://doi.org/10.1007/0-387-37625-9_1)
[38] Gueymard C A and Sengupta M 2012 Improving Modeled Solar Irradiance Historical Time Series: What is the Appropriate Monthly Statistic for Aerosol Optical Depth? *World Renewable Energy Forum January 2012* (Denver, CO: World Renewable Energy Forum)
[39] Alonso-Álvarez D *et al* 2018 Solcore: a multi-scale, Python-based library for modelling solar cells and semiconductor materials *J. Comput. Electron.* **17** 1099–123
[40] Gordon I *et al* 2017 The HITRAN2016 molecular spectroscopic database *J. Quant. Spectrosc. Radiat. Transfer* HITRAN2016 Special Issue **203** 3–69
[41] Vandaele A *et al* 1998 Measurements of the $NO_2$ absorption cross-section from 42 000 cm1 to 10 000 cm1 (238–1000 nm) at 220 k and 294 k *J. Quant. Spectrosc. Radiat. Transfer* Atmospheric Spectroscopy Applications 96 **59** 171–84
[42] Zhang M *et al* 2018 Aerosol optical properties and radiative effects: assessment of urban aerosols in central China using 10-year observations *Atmos. Environ.* **182** 275–85
[43] Norton M, Amillo A G and Galleano R 2015 Comparison of solar spectral irradiance measurements using the average photon energy parameter *Sol. Energy* **120** 337–44
[44] Betts T, Gottschalg R and Infield D 2002 Modelling spectral irradiation effects on single- and multijunction amorphous silicon photovoltaic devices *Conf. Record of the Twenty-Ninth IEEE Photovoltaic Conf. 2002*
[45] Luque A and Hegedus S 2003 *Handbook of Photovoltaic Science and Engineering* (New York: Wiley)
[46] Cuce E, Cuce P M and Bali T 2013 An experimental analysis of illumination intensity and temperature dependency of photovoltaic cell parameters *Appl. Energy* **111** 374–82
[47] ASTM International 2020 Standard Tables for Reference Solar Spectral Irradiances: Direct Normal and Hemispherical on 37° Tilted Surface (West Conshohocken, PA: STM) (https://doi.org/10.1520/G0173-03R20)